Nanoscale

PAPER

View Article Online
View Journal | View Issue

Cite this: *Nanoscale*, 2023, **15**, 18832

Cool carriers: triplet diffusion dominates upconversion yield

Colette M. Sullivan, †[a] Jason E. Kuszynski,†[a] Alexey Kovalev,[b] Theo Siegrist,[b,c] Richard D. Schaller,[d] Geoffrey F. Strouse [a] and Lea Nienhaus *[a]

Received 4th September 2023,
Accepted 3rd November 2023

DOI: 10.1039/d3nr04446g

rsc.li/nanoscale

Perovskites have gained popularity both as the active material in photovoltaics and as bulk triplet sensitizers for solid-state triplet–triplet annihilation upconversion (TTA-UC). Prior to widespread implementation into commercial photovoltaics, an in-depth understanding of the environmental influences on device performance is required. To this point, the temperature-dependent structure–function properties of TTA-UC within methylammonium formamidinium lead triiodide (MAFA)/rubrene UC devices are explored. A strong temperature dependence of the underlying UC dynamics is observed, where the maximum UC efficiency is achieved at 170 K, reflecting the competition between triplet diffusion length, diffusion rate, and triplet–triplet encounter events. A combination of spectroscopic and structural methods and theoretical modelling illustrates that despite the significantly increased carrier lifetime of the perovskite at low temperatures, the TTA-UC dynamics are not governed by the underlying sensitizer properties but rather limited by the underlying triplet diffusion.

Introduction

Photon upconversion (UC) has the potential to increase solar cell efficiencies by harvesting and subsequently utilizing sub-bandgap photons.[1–3] In contrast to second harmonic frequency generation[4–6] or lanthanide-based UC,[7–9] triplet–triplet annihilation (TTA) based methods benefit from becoming efficient at low, solar-relevant incident fluxes.[10–12] In TTA-UC, electronic coupling of two spin-triplet states (T_1) enables a spin-allowed process which ultimately generates a high energy excited singlet state (S_1) and a ground state (S_0).[13–16] As TTA relies on a large population of excited triplet states, and the direct optical transition from $S_0 \rightarrow T_1$ is a spin-forbidden process, triplet sensitizers are utilized.[17] To date, a wide variety of triplet sensitizers have been employed including metal–organic complexes with strong spin–orbit coupling,[16,18,19] nanocrystals,[10,20–24] transition metal dichalcogenides,[25–27] and bulk lead halide perovskites.[11,28–31]

Despite promising and high-efficiency results for solution-based UC,[15,32–35] similar success has not yet been transferred to solid-state applications due in large part to additional complications stemming from intermolecular interactions and back-transfer of the generated singlet states to the sensitizer due to the broadband absorption of *e.g.*, semiconductor nanocrystals and perovskites.[17] For eventual device integration, the underlying complexities in solid-state TTA-UC applications must be explored to continue to push the boundaries of this technology.

In real-world applications, major benefits of solution-processed perovskite-based upconversion devices would be their compatibility with flexible and lightweight substrates, enabling their integration into solar cells used in remote settings or possibly even in outer space applications.[36–39] A critical aspect of device integration for such applications is successful operation within environments harsher than the controlled laboratory environment. To this point, we recently investigated the effect of elevated temperatures (up to 60 °C) on perovskite-sensitized TTA-UC.[40] Under constant exposure to sunlight, solar cells are known to reach temperatures up to 85 °C, even in moderate climates. With the addition of an UC device, slightly lower temperatures are expected under operating conditions due to its location beneath the active photovoltaic. However, to understand their operation in climates with both elevated and at extreme low temperatures, the influence of both high and low temperature regimes must be understood.

Perovskites exhibit temperature-dependent carrier diffusion rates, changes to thermal carrier de-trapping rates, and excitonic behavior when the temperature is lowered such that ambient thermal energy is no longer sufficient to overcome the exciton binding energy.[41] Therefore, perovskites also

[a]*Department of Chemistry and Biochemistry, Florida State University, Tallahassee, FL 32306, USA. E-mail: lnienhaus@fsu.edu*
[b]*National High Magnetic Field Laboratory, Tallahassee, FL 32310, USA*
[c]*FAMU-FSU College of Engineering, Tallahassee, FL 32310, USA*
[d]*Center for Nanoscale Materials, Argonne National Laboratory, Lemont, IL 60439, USA*
† Equal contribution.

exhibit a strong temperature-dependence of the photoluminescence (PL) quantum yield (QY).[36,42–45] It is reasonable to assume that the triplet sensitization mechanism will also be highly dependent upon temperature in perovskite/rubrene bilayers. Further temperature-dependent complexity will arise from the known lead halide perovskite phase transition from a tetragonal unit cell to the orthorhombic unit cell between ~150–100 K.[46–48] This structural transition will impact the excited state frontier orbitals that influence the orbital overlap at the perovskite/rubrene interface, a fundamental requirement for the electron transfer governing the triplet generation process.

In addition to the temperature-dependent properties of the perovskite sensitizer, rubrene, the triplet annihilator, exhibits thermally activated singlet fission (SF) and therefore, a highly temperature-dependent PLQY.[49–51] Solid-state TTA-UC is inherently triplet diffusion based,[17,52,53] which can either follow a Marcus-type thermally activated triplet hopping model with strong temperature dependence,[54] or follow the disorder-driven Miller-Abrahams model at low temperatures, which exhibits a lesser temperature dependence.[55,56] Consequently, low temperatures are expected to influence both the perovskite sensitizer, as well as the dynamics and properties of TTA-UC.

To deconvolute the temperature-dependent effect of changes to the sensitizer and the annihilator in TTA-UC, methylammonium formamidinium lead triiodide ($MA_{0.85}FA_{0.15}PbI_3$) perovskite in the presence of rubrene (MAFArub) as well as properties of the rubrene annihilator are studied from 300 K to 20 K. The experimental studies demonstrate peak TTA-UC efficiency is achieved at 170 K, which is attributed to the competition between triplet diffusion length, diffusion rate, triplet–triplet encounters, and structural perturbation. The results suggest tuning of the molecular interactions and structure can provide a means to control the peak upconversion temperature. We have previously shown that for solution-processed UC devices, the dopant dye dibenzotetraphenylperiflanthene (DBP) does not play a significant role in the obtained brightness of UC. To avoid possible temperature-dependent effects from DBP harvesting the emissive rubrene singlet state *via* a Förster resonance energy transfer step,[57,58] here, rubrene is used as both the annihilator and emitter species to understand the properties of the upconverted emission stemming from the MAFArub UC devices.

Results and discussion

The influence of low temperature on both the perovskite sensitizer as well as rubrene annihilator within MAFArub bilayer UC devices is investigated. The absorption and emission properties of the bilayer film are monitored between 300 K and 20 K in steps of 10 K. In Fig. 1a and b, the expected redshift in both the perovskite absorption onset and the steady-state photoluminescence (PL) is observed. However, at ~110 K, the absorption onset rapidly blue shifts and splits into two distinct optical features. This redshift followed by a discrete jump in

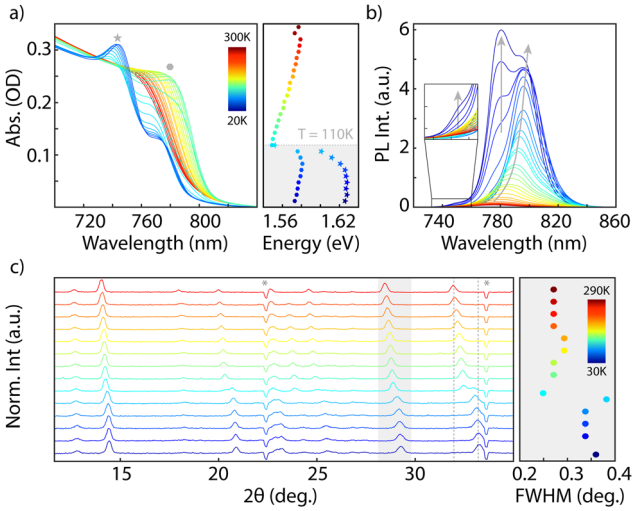

Fig. 1 (a) Temperature-dependent absorbance spectra (left) for the 100 nm MAFArub bilayer highlighting the changes to the perovskite onset as the film is cooled from 300 K to 20 K (red to blue). Bandgap extracted by Tauc plots (right) for the two phases, denoted by grey octagons and stars, with the phase transition at 110 K included. (b) Direct PL spectra for MAFArub bilayer cooling from 300 K to 20 K collected under 405 nm excitation. Three spectra were collected at each temperature then averaged. Spectral inset highlights the growth of the high energy feature at 750 nm. Grey arrows are included as guides to the eye. (c) MAFArub XRD patterns (left) collected from 290 K to 30 K. The asterisks denote instrumental artifacts. Grey dashed lines are included to highlight peak change. Calculated full-width at half-max (FWHM) for the (220) plane across the temperature range.

the optical bandgap has been previously investigated in perovskites and assigned to a phase transition from the tetragonal to the orthorhombic perovskite phase.[46,48,59] The absorption and emission features split (Fig. 1a and b) into multiple transitions during the phase transition from the tetragonal to orthorhombic crystal structure at ~110 K, which is unaffected by the presence of rubrene (Fig. 1c). Probing the underlying perovskite structure within the MAFArub bilayers *via* temperature dependent X-ray diffraction (XRD) studies shows broadening of the perovskite reflections (Fig. 1c, right) occurring post-phase transition indicative of an increase in disorder. The splitting of the optical absorption and emission post-phase transition can be correlated to phase segregation of the mixed cation perovskite, leading to methylammonium-richer ($MA_{0.85+x}FA_{0.15-x}PbI_3$) and formamidinium-richer ($MA_{0.85-x}FA_{0.15+x}PbI_3$) domains, of which the former exhibits a slightly larger bandgap than the latter.[60] In addition, a third high energy peak appears at 750 nm post-phase transition which has been previously attributed to the orthorhombic phase within $CH_3NH_3PbI_3$ thin-films.[42]

To investigate the influence of temperature on the UC process, as well as the rubrene layer itself, the emission from rubrene in MAFArub was investigated under both 780 nm excitation (upconverted emission, Fig. 2a) and 405 nm excitation (direct emission, Fig. 2b). The upconverted emission is observed to sharply increases in intensity when the tempera-

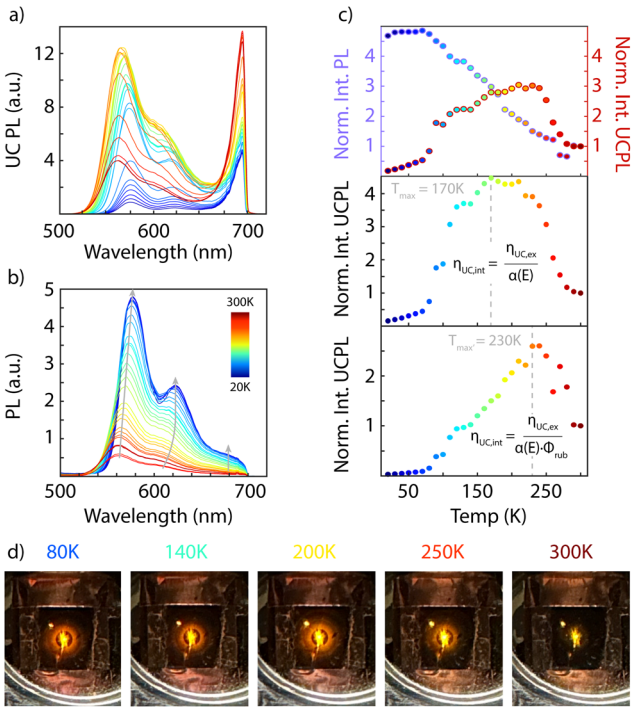

Fig. 2 (a) UCPL for the 100 nm MAFArub bilayer collected under 780 nm (150 W cm^{-2}) excitation while cooling from 300 K to 20 K where three spectra were collected at each temperature then averaged. (b) Direct emission of the MAFArub bilayer under 405 nm excitation collected while cooling from 300 K to 20 K. A 700 nm short-pass filter was used to isolate the dye emission. Three spectra were collected at each temperature then averaged. Grey arrows are included as guides to the eye. (c) (top) Integrated direct (lavender) and upconverted (red) emission for the bilayer film. (middle) Integrated UCPL ($\eta_{UC,ex}$) normalized to the absorption overlap of the bilayer film with the excitation laser ($\alpha(E)$). The dashed grey line represents T_{max} = 170 K. (bottom) The absorption normalized, integrated UCPL spectra normalized by the quantum yield of rub under direct excitation, with the equation included. Here, $T_{max'}$ is 230 K, indicated *via* the dashed grey line. (d) Photographs of the MAFArub bilayer under 780 nm excitation at select temperatures.

ture is initially lowered. At 230 K, the maximal upconverted intensity is reached, after which the upconverted PL intensity slowly drops before a significant reduction in upconverted emission is observed below 90 K (Fig. 2c, top).

The observed UC behavior in the bilayer in Fig. 2 is complicated by a set of temperature dependent behaviors that impact the relative external ($\eta_{UC,ex}$) and internal ($\eta_{UC,int}$) UC yield. The 'external' upconversion efficiency $\eta_{UC,ex}$ (incident photons *vs.* upconverted photons) is evaluated by considering the triplet generation efficiency based on charge transfer (η_{ET}), the efficiency of TTA (η_{TTA}), as well as the QY of rubrene (η_{rub}), all of which dictate the fraction of TTA-generated singlet states that subsequently relax through radiative recombination, as shown below in eqn (1).

$$\eta_{UC,ex} \propto \eta_{ET}\eta_{TTA}\eta_{rub} \quad (1)$$

The 'internal' UC efficiency ($\eta_{UC,int}$) is dependent on the absorption cross section $\alpha(E)$ of the perovskite sensitizer at the excitation wavelength of 780 nm. Due to the observed strong temperature dependence of the perovskite absorption onset (*vide supra*), we expect a significant impact on the yield of UC. Hence, to decouple the varying excitation density from the UC yield, $\eta_{UC,ex}$ is normalized by the overlap integral of the 780 nm excitation laser and the perovskite absorption $\alpha(E)$ (Fig. 2c, middle).

$$\eta_{UC,int} = \eta_{UC,ex}/\alpha(E) \quad (2)$$

The same general trend holds, where the internal UC efficiency first increases to T_{max} = 170 K and then rapidly decreases after the perovskite phase transition at 110 K.

Since SF in rubrene is also known to be thermally activated, reducing the available ambient thermal energy by cooling the sample will result in a reduction of the rate of SF and thereby increase the QY of rubrene under direct excitation (Fig. 2b).[49,51] To decouple the underlying QY of the annihilator from the TTA-UC process of interest here, the upconverted PL intensity is further normalized by the underlying rubrene PL intensity Φ_{rub} (Fig. 2c, bottom).

$$\eta_{UC,int} = \eta_{UC,ex}/(\alpha(E)\Phi_{rub}) \quad (3)$$

After decoupling both the sensitizer absorption cross section as well as the annihilator emission QY, the UC intensity peaks at $T_{max'}$ = 230 K after which a gradual roll-off is found. This highlights that room temperature is not the ideal temperature for TTA-UC in this system.

To ensure that the changes in the peak UCPL intensity are not simply due to a change in the intensity threshold I_{th}, the power dependence of the UCPL is investigated at different temperatures. The I_{th} describes the incident power at which TTA-UC becomes the dominant triplet decay pathway,[61] and the TTA-UC process becomes efficient. For excitonic systems, this is found as the point where the UCPL changes from a quadratic power dependence to a linear power dependence. On a log–log plot, this amounts to a change in slope from α = 2 to α = 1. However, in the case of perovskite-sensitized UC, we have found the underlying perovskite PL power dependence I^{α} to be critical, which is determined by the competition of bimolecular (non-geminate) and monomolecular (trap-assisted) charge carrier recombination;[11] here, a change in slope from $2 \times I^{\alpha}$ to I^{α} is found. Above the linear regime, the saturation regime shows a diminished power dependence, where the UCPL increases sub-linearly with increasing power. Fig. 3 shows the power dependence at the key points: room temperature, near T_{max} (200 K is chosen as it is the average between T_{max} and $T_{max'}$), and at 80 K, below which the UCPL intensity strongly diminishes and approaches zero.

The results indicate that the I_{th} is directly related to the observed UC intensity: a higher UC intensity is related to a lower intensity threshold. However, since all steady-state UCPL measurements are performed well above the I_{th}, the change in the threshold power cannot be the underlying cause of the change in the UC efficiency.

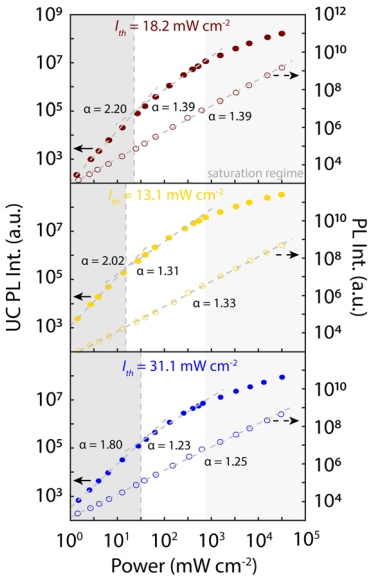

Fig. 3 Temperature-dependent power-dependent UCPL (filled) and perovskite PL (rings) for the MAFA/rub bilayer under 780 nm excitation for 300 K (top), 200 K (middle), and 80 K (bottom). The intersection of the dashed grey lines for the two regimes yields the intensity threshold (I_{th}, dark grey box) at all the three temperatures. The saturation regime of the UCPL is indicated by the light grey box.

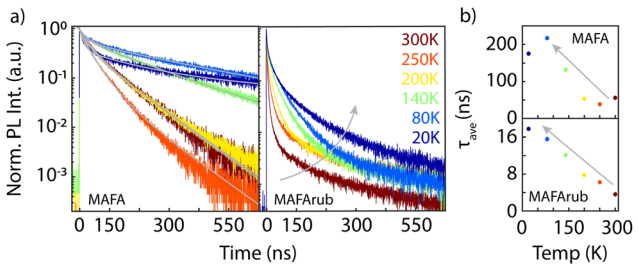

Fig. 4 (a) Temperature-dependent perovskite PL decays for the neat MAFA film (left) and MAFArub bilayer (right) collected under 635 nm pulsed excitation (125 kHz). Triexponential fits are included as grey lines for the MAFA decays. The grey arrow is included as a guide to the eye for the MAFArub decays. (b) Amplitude-weighted average lifetimes (τ_{ave}) for the MAFA (top) and MAFArub (bottom) films. Grey arrows are included as guides to the eye.

To further understand the underlying cause of this increase in the UC efficiency at low temperatures, the dynamics of the perovskite PL in absence and in presence of the annihilator (Fig. 4a and b) are investigated. The resulting PL decays are fit to a triexponential function to fully capture the complex dynamics occurring.

$$I(t) = A_1 \cdot \exp^{\frac{-t}{\tau_1}} + A_2 \cdot \exp^{\frac{-t}{\tau_2}} + A_3 \cdot \exp^{\frac{-t}{\tau_3}} \quad (4)$$

The resulting lifetimes and amplitude-weighted average lifetimes $\tau_{ave} = \frac{\sum A_i \tau_i}{\sum A_i}$ are plotted in Fig. 4b and tabulated in Table 1.

In agreement with previous reports, a general increase of the perovskite PL lifetime with decreasing temperature (Fig. 4a) is found.[42] Below the phase transition at ~110 K, an additional rapid early time component is present, possibly due to generation of deep traps during the phase transition and phase segregation or varying emission rates from the different emissive species. In the presence of rubrene, the lifetime monotonically increases from 3.6 ns at 300 K to 17.7 ns at 20 K (Fig. 4b, bottom). However, in comparison to the neat perovskite, the PL dynamics are considerably quenched, indicating charge extraction at the perovskite/rubrene interface.

While quenching of the perovskite PL dynamics at early times does support that triplet states are generated in rubrene, it can also simply be explained by hole extraction. To further support the hypothesis for triplet generation, temperature-dependent ultrafast transient absorption spectroscopy is utilized to investigate the triplet generation process at the perovskite/rubrene interface (Fig. 5). In order to reduce the signal from the bulk of the perovskite sensitizer, we utilize 30 nm thick perovskite layers here rather than aforementioned 100 nm films used for the steady-state investigations. To complete the picture of the underlying temperature dependence, MAFArub data at temperatures higher than 300 K is also included.[40] We have previously shown that the characteristic excited state absorption (ESA) correlated to the spin allowed $T_1 \rightarrow T_3$ transition in rubrene appears within the first nanosecond after excitation at room temperature.[62,63] Comparing the absorption spectra of the perovskite/rubrene bilayer at selected delay times for 340 K, 295 K, 200 K, and 80 K, the expected perovskite-related ground state bleach (GSB), perovskite-related photobleach appearing at higher energy (PB2), perovskite photoinduced absorption (PIA), as well as the emergence of the rubrene $T_1 \rightarrow T_3$ excited state absorption (ESA) are observed across all investigated temperatures (Fig. 5a).[62] To compare the optical density of the rubrene triplet ESA, the absorption spectrum after 4 ns is extracted at each temperature

Table 1 Fitting parameters for MAFA (left) and MAFArub (right, italics) perovskite PL decays based on a triexponential fit and the amplitude-weighted average lifetime

Temp (K)	A_1		τ_1 (ns)		A_2		τ_2 (ns)		A_3		τ_3 (ns)		τ_{ave} (ns)	
300	0.2	*1.0*	3.1	*2.1*	0.45	*0.05*	42.5	*12.6*	0.4	*0.005*	100	*177*	**55.6**	***3.4***
250	0.2	*0.8*	4.8	*2.0*	0.7	*0.2*	39	*11.4*	0.1	*0.01*	100	*161*	**38.5**	***5.9***
200	0.2	*0.7*	4.6	*1.8*	0.4	*0.3*	37.6	*13.3*	0.4	*0.01*	102	*128*	**53.2**	***7.8***
140	0.3	*0.7*	20.3	*2.4*	0.6	*0.3*	186	*20.1*	0.02	*0.04*	1000	*100*	**143**	***11.6***
80	0.4	*0.6*	27	*2.6*	0.5	*0.3*	230	*23*	0.07	*0.07*	1000	*87*	**236**	***15.1***
20	0.6	*0.6*	12.7	*2.2*	0.2	*0.3*	153	*18.5*	0.1	*0.1*	1000	*108*	**186**	***17.1***

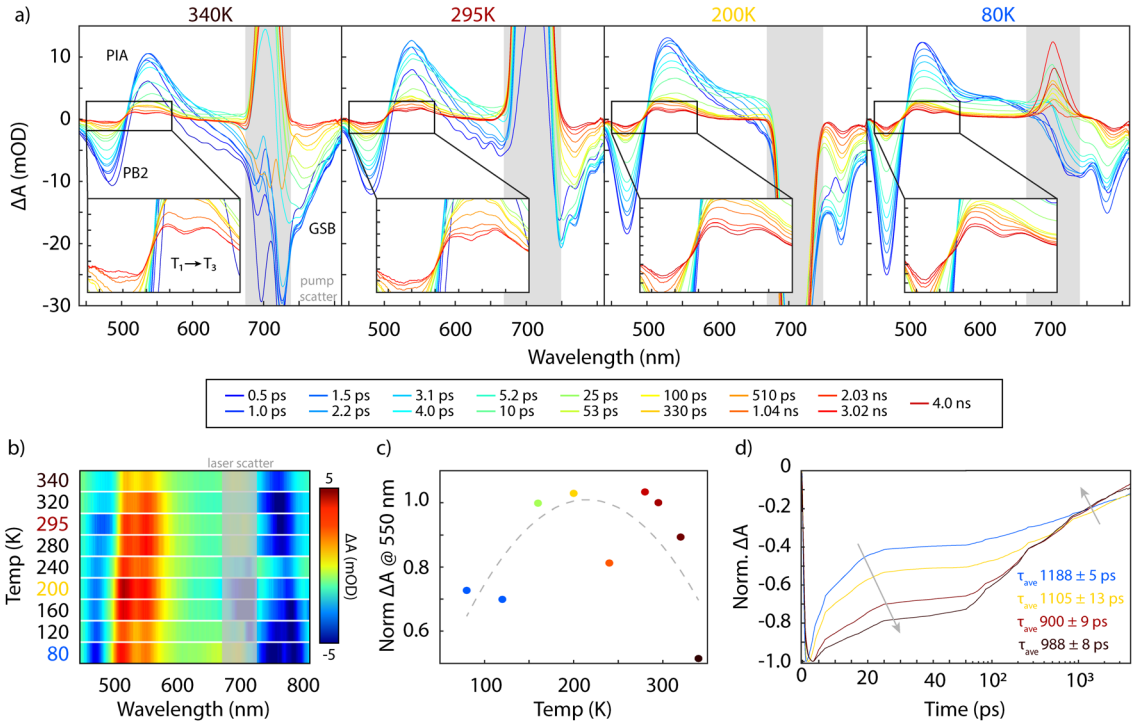

Fig. 5 (a) Temperature-dependent transient absorption spectra extracted at specific delay times for a MAFArub bilayer film with a thinner perovskite (30 nm) to allow a sufficient signal-to-noise ratio under 700 nm pump at a pulse power of 23.6 mJ cm^{-2}. The characteristic perovskite high energy photobleach (PB2), ground state bleach (GSB), and photoinduced absorption (PIA) features are labeled. The rub $T_1 \rightarrow T_3$ transition at 510 nm is included in the spectral inserts. Excess pump scattering is denoted *via* the grey box. (b) The raw spectra for MAFArub extracted at 4 ns across the different temperatures under 700 nm pump at a pulse power of 7.8 mJ cm^{-2}. Pump scattering is denoted by the grey box. (c) ΔA values extracted at 550 nm for the different spectra are shown in (b) normalized to the value at 295 K. The grey curved trace is included as a guide for the eye. (d) GSB kinetics for the four temperatures shown in (a), with the amplitude weighted average lifetimes included. Grey arrows are included as guides.

(340 K to 80 K) (Fig. 5b). Only slight differences to the triplet-related signal are found, indicating that the rapid drop-off observed in the UCPL below 100 K is unrelated to the efficiency of interfacial triplet generation (Fig. 5c). Lastly, we investigate the temperature-dependent recovery of the perovskite GSB (Fig. 5d). At low temperatures, the GSB recovers rapidly within the first 100 ps and slower at later times, which can likely be correlated to a higher fraction of rapid excitonic recombination in the perovskite at lower temperatures at early times, followed by a reduction in the rate of free charge carrier recombination.

Finally, the kinetics of the upconverted PL are considered. Due to the rapid nature of the actual TTA-UC process, the upconverted PL dynamics are rate-limited by the underlying triplet diffusion kinetics, yielding the delayed rise in the UCPL. At later times however, the upconverted PL dynamics are rate limited by the lifetime of the excited triplet state. We have previously observed that the rise time of the upconverted PL dynamics is closely tied to the triplet population density,[53] and two distinct TTA-UC processes can occur: rapid UC at the interface and diffusion-mediated TTA-UC further from the interface, where the latter has a higher apparent QY due to reduced singlet back transfer to the perovskite sensitizer. Fig. 6a shows the normalized upconverted PL kinetics with their corresponding fits, offset for ease of comparison. The extracted rises and decays for the UCPL decays are tabulated in Table 2. The first four temperatures (300 K to 140 K) were fit to single exponential terms for both the rise and decay components while the 80 and 20 K lifetimes were better fit with a biexponential rise. Of note is for the lowest temperature 20 K, 40% of the upconverted PL rise occurs in the first 200 ns, indicating a significant amount of the triplet states rapidly undergo TTA-UC without diffusion. Since triplet generation at the perovskite/rubrene interface and TTA-UC are known to be (ultra-)fast processes, slow diffusion to a triplet encounter is the rate-limiting process for TTA-UC away from the interface and as a consequence, the slow rise into the peak emission can be used as a proxy for the rate of triplet diffusion. As expected, based on an Arrhenius-type triplet hopping mechanism with an activation energy E_a, the rate of diffusion initially slows with decreasing temperature T (Fig. 6b).

$$k_{hop} = A \cdot \exp\left(-\frac{E_a}{kT}\right) \quad (5)$$

The UCPL rise time noticeably slows from 0.60 to 1.56 μs between 300 K and 140 K, yielding an activation barrier of 21.4 meV for triplet diffusion. Interestingly, the rise accelerates below 140 K, which could be indicative of a change in

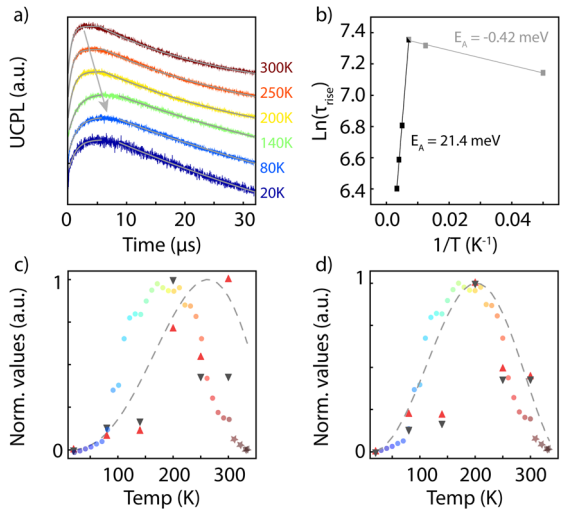

Fig. 6 (a) UCPL dynamics for the 100 nm MAFArub film for the specified temperatures under 780 nm excitation at an average power density of 19 mW cm^{-2}. Each decay is normalized to the maximum and offset for clarity, fits are shown as solid lines. (b) The triplet rise times are compared in an Arrhenius plot, where the four highest temperatures are linearly related with an activation energy of 21.4 meV associated with the energy barrier for an Arrhenius-type hopping mechanism. The lowest temperatures feature a negligible activation energy of −0.4 meV, indicative of a transition to an energetically favorable Miller-Abrahams-type regime. (c) Normalized UCPL model following an inverse temperature dependence for the diffusion length, similar to triplet behavior observed previously in anthracene (dashed grey curve).[68] The dark grey triangles utilize experimental triplet decay lifetimes while the red triangles are triplet rise lifetimes. (d) The same normalized UCPL compared with a similar diffusion model using an empirical diffusion model (dashed grey curve) ($I_{UC} \propto k_{TTA} = 8\pi D_T R_{TT} T_E$) where the triplet diffusivity is a convolution of a linearly temperature dependent triplet lifetime, a square root temperature dependent diffusion length, and the experimentally measured triplet density trend. The higher temperature data points indicated *via* stars in both (c) and (d) were extracted from data related to ref. 40.

Table 2 Extracted decays and rises for the MAFArub UCPL traces based on a single exponential fits to the rise and decay for 300 K to 140 K and a biexponential rise for 80 K and 20 K

Temp (K)	τ_{decay} (μs)	A_1	τ_{rise} (μs)	A_2	τ_{rise} (ns)
300	23.11	—	0.60	—	—
250	29.20	—	0.73	—	—
200	33.91	—	0.90	—	—
140	67.56	—	1.56	—	—
80	75.13	0.77	1.51	0.23	107
20	79.22	0.60	1.27	0.4	83.4

diffusion mechanism from the Arrhenius-type activated triplet hopping to a disorder mediated Miller-Abrahams model at very low temperatures, or simply be an artifact caused by an increased triplet density near the interface due to reduced triplet movement. Thermal contraction of the crystal lattice and a first-order phase transition impacting the herringbone slip-stacking has also been observed in rubrene at ~200 K, which has been shown to influence the intermolecular coupling.[64] As a result, the triplet diffusion rate k_{hop} would be influenced according to Fermi's golden rule (eqn (6)):[52]

$$k_{hop} = k_{if} = \frac{2\pi}{\hbar}|J_{if}|S_{if} \quad (6)$$

where J_{if} describes the electronic coupling and S_{if} the overlap integral of the vibronic state of the initial and final state. The late time UCPL decay, then, is rate-limited by the effective triplet lifetime which decreases with increasing temperature, indicating additional triplet relaxation pathways at elevated temperaures.[65]

A theoretical model can be generated from first-principal temperature dependencies where no fit minimization is performed to support the observed temperature-dependent upconverted PL intensity. Data points for MAFArub at temperatures above 300 K are included to ensure the model matches the behavior at all temperatures of interest.[40] The UCPL intensity (I_{UC}) is dependent upon the PL QY of the annihilator (Φ_{PL}), triplet population (N_A), overall lifetime of the triplet annihilator (k_T), and bimolecular rate constant describing TTA k_{TTA}.[52,66,67]

$$I_{UC} = \int_0^\infty \Phi_{PL} \frac{k_{TTA}[N_A]^2}{2k_T}. \quad (7)$$

In solid-state UC systems, I_{UC} is proportional to k_{TTA}, which can further be described as the product of the triplet diffusivity (D_T), the effective annihilation distance (R_{TT}), and triplet population (N_A):[52]

$$I_{UC} \propto k_{TTA} = 8\pi D_T R_{TT} N_A \quad (8)$$

Due to the short-range nature of the wavefunction overlap required for TTA-UC, the effective annihilation distance R_{TT} is estimated at 1 nm.[52] The triplet diffusivity D_T for three dimensional diffusion is related to the diffusion length (L) and the triplet lifetime (τ_T):

$$D_T = \frac{L^2}{6\tau_T}. \quad (9)$$

The trend in the relative triplet population (N_A) is estimated based on the optical density of the rubrene PIA at 550 nm (Fig. 5c), where a slight temperature dependence is found in the investigated temperature range despite the 80-fold increase in the perovskite PL QY and 3-fold increase in the perovskite PL lifetime. These findings emphasize that the limiting factor for triplet generation at the perovskite/rubrene interface is not the perovskite PL lifetime nor perovskite QY. The triplet lifetime (τ_T) is approximated by the decay time of the upconverted PL ($\tau_T \propto |-T|$) (Table 2). If the temperature dependence of the triplet diffusion length (L) in rubrene is assumed to mimic a similar trend as in anthracene ($L \propto |-T^{-1}|$) where a strong temperature dependence is found at low temperatures and a lesser dependence at higher temperatures,[68,69] the model quickly fails at temperatures above 50 K (Fig. 6c).

To reconcile the turnover in the upconverted PL intensity above T_{max} = 170 K, additional thermally activated pathways

which reduce the number of triplets available for TTA-UC are required.[70,71] Increased temperature will increase triplet diffusion rates based on thermally activated hopping, which results in triplets reaching quenching sites more rapidly and reduces the effective triplet diffusion length, L.[40] As a result, with increasing temperatures, an increasing portion of the initially generated triplet states will be quenched *via* other pathways rather than the desired bimolecular TTA-UC pathway, leading to a decrease in the available triplet population at time t.[67]

$$\frac{d[N_A]_t}{dt} = -k_Q[N_A]_t - k_{TTA}[N_A]_t^2 \quad (10)$$

Here, k_Q is the rate for additional unimolecular triplet quenching pathways. In the strong annihilation limit, substitution of the analytical solution of eqn (10) into eqn (7) yields a simple direct proportionality of the upconversion intensity on the triplet population.[67]

$$I_{UC} \propto [N_A], \quad (11)$$

Hence, the additional triplet decay pathways at elevated temperatures will strongly reduce the available triplet population which is reflected in the observed TTA-UC efficiencies at temperatures above T_{max} = 170 K. Compared to a hopping-free anthracene, L is adjusted to approximate the expected temperature dependence for a trap-based model for TTA-UC at the perovskite/rubrene interface. The proposed change in L is also in agreement with other observations of charge-carrier recombination dynamics in $CH_3NH_3PbI_3$.[72]

Fig. 5d shows the agreement of the adjusted model compared to the experimental data when including a triplet diffusion length reducing with increasing temperature $\left(L \propto \left|\sqrt{-T}\right|\right)$.[73] Comparing both modeling results to the experimental data, we find that the triplet diffusion length is critical to understanding UCPL dynamics as a function of temperature and should be investigated for future temperature dependent studies. For further model validation, the experimentally determined triplet lifetime rises (τ_{rise}, red triangles) and decays (τ_{decay}, dark grey triangles) from Table 2 are used to estimate the expected UCPL trend more precisely (Fig. 6c and d). Using the experimental lifetimes, the anthracene-based model fails above 80 K as observed previously with the diffusion length modeling, and very good agreement for the adjusted model at all temperatures, except for 140 K. We hypothesize that as 140 K is near the suspected transition between Arrhenius-type activated hopping and Miller-Abrahams mediated disorder, the model underestimates UCPL in this region.

Conclusion

In summary, we observe a strong temperature-dependence of the upconverted PL QY for the MAFArub system. Interestingly, the strong temperature dependence is not related to temperature-dependent changes in the perovskite properties, rather it can be explained by a change in the triplet diffusion underlying TTA-UC. Despite the high rubrene QY at low temperatures due to suppressed thermally activated SF, we find that the rate of triplet collisions is greatly reduced due to a reduction in the triplet diffusion rate. At temperatures above T_{max}, the upconverted PL QY is reduced due to increased triplet quenching, which yields a reduced triplet population available for TTA-UC. Importantly, these results highlight that for the perovskite-sensitized system explored here, temperatures below 298 K are ideal for TTA-UC, and that longer perovskite PL lifetimes at low temperatures do not increase the yield of TTA-UC despite longer lived carriers. Hence, the carrier lifetime in the perovskite is not the limiting factor for triplet generation.

Experimental

Film fabrication

Glass substrates were cleaned *via* sonication in the following solutions for 15 min: 2% Hellmanex, deionized water, ethanol, and acetone. The substrates were placed in a UV-ozone plasma cleaner (Ossila) for 15 min. Precursor solutions of 1.2 M methylammonium iodide (MAI, Dyenamo) and formamidinium iodide (FAI, Dyenamo) were dissolved in a solution of DMF/DMSO (9 : 1 *v*/*v*, Sigma) containing lead iodide. Precursor solutions were diluted to either half or one fifth of the original concentration to make the ~100 and ~30 nm films, respectively. The precursor solutions were spin coated using a two-step program: 1000 rpm for 10 s and 5000 rpm for 30 s. Chlorobenzene (Sigma) was used as the antisolvent, and the thin films were annealed at 100 °C for 15 min. To fabricate MAFArub bilayer films, rubrene (rub, 10 mg mL^{-1}) in anhydrous toluene (Sigma) was spin-coated onto the perovskite post-fabrication at 6000 rpm for 20 s. All films were encapsulated in an inert nitrogen-filled glovebox using two-part epoxy (Devcon).

For the temperature-dependent XRD studies, bilayer films were deposited onto sapphire substrates in an effort to minimize background.

Steady-state optical spectroscopy

All visible absorption spectra were collected using a Thermo Scientific Evolution 220 spectrophotometer.

Steady-state PL spectra were collected by an Ocean Optics spectrometer (HR2000 + ES). Direct excitation emission for all films were collected *via* a 405 nm continuous wave laser (LDH-D-C-405, PicoQuant) at 0.6 mW. Excess laser scatter was removed *via* a 425 long-pass filter (Chroma Tech.). Upconverted emission for the MAFA/rub bilayers were collected using a 780 nm continuous wave laser (LDH-D-C-780, PicoQuant) at 30 mW (200 μm spot size). A 700 nm short-pass filter (ThorLabs) was used to isolate the upconverted emission.

Time-resolved photoluminescence spectroscopy

Time-resolved PL measurements for the perovskite PL decays were collected under 635 nm picosecond pulsed excitation (LDH-P-C-635 M, PicoQuant) at 125 kHz and 4.3 μW. An 800 nm long-pass filter (ThorLabs) and 633 nm notch (ThorLabs) were used to isolate the perovskite PL and minimize laser scattering. Upconverted PL decays were measured under 780 nm picosecond pulsed excitation (LDH-D-C-780, PicoQuant) at 32.25 kHz and 3.8 μW. A 650 nm short pass (ThorLabs) and 700 nm short pass (ThorLabs) filters were used to isolate the UCPL and remove excess laser scatter. The single photon counting avalanche photodiode used was from Micro Photon Devices, and all collected PL decays were histogrammed by a HydraHarp 400 (PicoQuant) event timer.

Power-dependent PL measurements

Both UCPL and perovskite PL power dependencies for the MAFArub bilayer were collected under 780 nm continuous wave excitation (LDH-D-C-780, PicoQuant). A silicon power meter (PM100-D, ThorLabs) was used to measure the laser powers, and neutral density filters (ThorLabs) were used to attenuate powers. For the perovskite PL, a 780 nm notch (ThorLabs) and 800 nm long-pass filter (ThorLabs) were used to remove excess laser scatter. A combination of a 780 nm notch (ThorLabs), 700 nm short-pass (ThorLabs), and 650 nm short-pass (ThorLabs) were used to isolate UC emission and remove laser scattering. All photon arrival times were counted for 20 s by a HydraHarp 400 (PicoQuant) event timer with a single-photon avalanche photodiode (Micro Photon Devices). The spot size (200 μm) was determined using a razor blade.

Temperature control

Temperature control for steady-state and time-resolved emission studies were achieved *via* a He-filled cryocooler (Air Products). Encapsulated films were mounted onto a cold-finger optical sample mount prior to sheath evacuation ($\sim 10^{-5}$ mBar) where a PID Digital Temperature Controller Model 9650 (Scientific Instruments) was used to attain and maintain desired temperature. For each temperature point, the cold-finger was left to equilibrate for approximately 1 min prior to collecting absorbance and PL spectra.

Transient absorption spectroscopy

Transient absorption was performed using an 800 nm, 35 fs pulse width, 2 kHz, amplified titanium : sapphire laser (Spectra Physics, Spitfire). White light probe pulses were produced by focusing a portion of the output into a 2 mm thick sapphire crystal following a time delay that was controlled using a mechanical delay stage and retroreflector. Pump pulses were produced using an optical parametric amplifier (Light Conversion, TOPAS) that afforded tunable near-infrared light, which was then converted into red photons *via* harmonic generation. The pump was reduced to 1 kHz repetition rate using a mechanical chopper. Both pump and probe were focused and overlapped on the sample with the pump spot exceeding twice the diameter of the probe. Probe pulses were spectrally dispersed after passing through the sample and compared for pump on *versus* pump off intensity on a single shot basis. All data was collected under a 700 nm pump at either 6 mW (180 μm spot size, Fig. 5a and d) or 4.12 mW (260 μm spot size, Fig. 5b and c).

X-ray diffraction

The XRD diffraction experiments were performed using a Rigaku UltraX-18 rotating anode generator with Cu source. The X-ray radiation from the source passed through an elliptic mirror, specifically designed for the Cu K_α wavelength (AXO Dresden GmbH, $f1$ = 350 mm, $f2$ = 3500 mm), to increase the signal intensity. The reflections were measured using a hybrid pixel area detector (DECTRIS Pilatus 300k wide) with the pixel size of 0.172 × 0.172 mm^2. The distance from the sample to the detector was about 430 mm along the normal to the plane of the detector. The sample was placed in vacuum and mounted on a copper sample holder inside a Displex 201 closed-cycle cryocooler with Be walls for X-ray transparency. During the measurements, the sample orientation with respect to incoming beam was determined by optimizing the observed peak.

Author contributions

Colette M. Sullivan: investigation, formal analysis, visualization, writing – review & editing. Jason E. Kuszynski: investigation, formal analysis, writing – review & editing. Alexey Kovalev: investigation. Theo Siegrist: investigation, formal analysis, writing – review & editing. Richard D. Schaller: investigation, formal analysis, writing – review & editing. Geoffrey F. Strouse: formal analysis, supervision, writing – review & editing. Lea Nienhaus, conceptualization, investigation, formal analysis, supervision, funding acquisition, writing – original draft, writing – review & editing.

Data availability

The raw data is available at **https://doi.org/10.17605/OSF.IO/K6SVM**.

Conflicts of interest

FSU has filed a provisional application for a US patent based on this technology that names L. N. as an inventor.

Acknowledgements

C. M. S. and L. N. acknowledge funding by the National Science Foundation under Grant No. DMR-2237977 and the Camille and Henry Dreyfus Foundation (TC-23-050). J. E. K. and G. F. S. acknowledge the National Science Foundation under Grant No. DMR-1905757. J. E. K. acknowledges the U.S. Department of

Defense SMART scholarship funded under OUSD/R&E, NDEP/BA-1. A. S. and T. S. performed part of the work at the National High Magnetic Field Laboratory, which is supported by the National Science Foundation under grant DMR-2128556 and the State of Florida. T. S. acknowledges funding by the National Science Foundation under grant DMR-2219906. Work performed at the Center for Nanoscale Materials, a U.S. Department of Energy Office of Science User Facility, was supported by the U.S. DOE, Office of Basic Energy Sciences, under Contract No. DE-AC02-06CH11357.

References

1 T. F. Schulze and T. W. Schmidt, *Energy Environ. Sci.*, 2014, **8**, 103–125.
2 T. F. Schulze, J. Czolk, Y.-Y. Cheng, B. Fückel, R. W. MacQueen, T. Khoury, M. J. Crossley, B. Stannowski, K. Lips, U. Lemmer, A. Colsmann and T. W. Schmidt, *J. Phys. Chem. C*, 2012, **116**, 22794–22801.
3 Y. Y. Cheng, B. Fückel, R. W. MacQueen, T. Khoury, R. G. C. R. Clady, T. F. Schulze, N. J. Ekins-Daukes, M. J. Crossley, B. Stannowski, K. Lips and T. W. Schmidt, *Energy Environ. Sci.*, 2012, **5**, 6953–6959.
4 N. Thantu, *J. Lumin.*, 2005, **111**, 17–24.
5 N. M. Lawandy and R. L. MacDonald, *J. Opt. Soc. Am. B*, 1991, **8**, 1307–1314.
6 E. V. Makeev and S. E. Skipetrov, *Opt. Commun.*, 2003, **224**, 139–147.
7 Q. Tian, W. Yao, W. Wu, J. Liu, Z. Wu, L. Liu, Z. Dai and C. Jiang, *ACS Sustainable Chem. Eng.*, 2017, **5**, 10889–10899.
8 K. W. Krämer, D. Biner, G. Frei, H. U. Güdel, M. P. Hehlen and S. R. Lüthi, *Chem. Mater.*, 2004, **16**, 1244–1251.
9 S. Heer, K. Kömpe, H.-U. Güdel and M. Haase, *Adv. Mater.*, 2004, **16**, 2102–2105.
10 M. Mahboub, Z. Huang and M. L. Tang, *Nano Lett.*, 2016, **16**, 7169–7175.
11 S. Wieghold, A. S. Bieber, Z. A. VanOrman, L. Daley, M. Leger, J.-P. Correa-Baena and L. Nienhaus, *Matter*, 2019, **1**, 705–719.
12 M. Wu, T.-A. Lin, J. O. Tiepelt, V. Bulović and M. A. Baldo, *Nano Lett.*, 2021, **21**, 1011–1016.
13 C. A. Parker, C. G. Hatchard and E. J. Bowen, *Proc. R. Soc. London, Ser. A*, 1997, **269**, 574–584.
14 T. N. Singh-Rachford and F. N. Castellano, *J. Phys. Chem. A*, 2008, **112**, 3550–3556.
15 T. N. Singh-Rachford and F. N. Castellano, *Coord. Chem. Rev.*, 2010, **254**, 2560–2573.
16 T. W. Schmidt and F. N. Castellano, *J. Phys. Chem. Lett.*, 2014, **5**, 4062–4072.
17 J. Alves, J. Feng, L. Nienhaus and T. W. Schmidt, *J. Mater. Chem. C*, 2022, **10**, 7783–7798.
18 V. Gray, A. Dreos, P. Erhart, B. Albinsson, K. Moth-Poulsen and M. Abrahamsson, *Phys. Chem. Chem. Phys.*, 2017, **19**, 10931–10939.
19 K. Börjesson, P. Rudquist, V. Gray and K. Moth-Poulsen, *Nat. Commun.*, 2016, **7**, 12689.
20 C. Mongin, S. Garakyaraghi, N. Razgoniaeva, M. Zamkov and F. N. Castellano, *Science*, 2016, **351**, 369–372.
21 L. Nienhaus, M. Wu, N. Geva, J. J. Shepherd, M. W. B. Wilson, V. Bulović, T. Van Voorhis, M. A. Baldo and M. G. Bawendi, *ACS Nano*, 2017, **11**, 7848–7857.
22 S. Garakyaraghi, C. Mongin, D. B. Granger, J. E. Anthony and F. N. Castellano, *J. Phys. Chem. Lett.*, 2017, **8**, 1458–1463.
23 J. A. Bender, E. K. Raulerson, X. Li, T. Goldzak, P. Xia, T. Van Voorhis, M. L. Tang and S. T. Roberts, *J. Am. Chem. Soc.*, 2018, **140**, 7543–7553.
24 Z. Huang, Z. Xu, M. Mahboub, X. Li, J. W. Taylor, W. H. Harman, T. Lian and M. L. Tang, *Angew. Chem.*, 2017, **129**, 16810–16814.
25 R. Dziobek-Garrett, C. J. Imperiale, M. W. B. Wilson and T. J. Kempa, *Nano Lett.*, 2023, **23**(11), 4837–4843.
26 S. Maiti, D. Poonia, P. Schiettecatte, Z. Hens, P. Geiregat, S. Kinge and L. D. A. Siebbeles, *J. Phys. Chem. Lett.*, 2021, **12**, 5256–5260.
27 J. Duan, Y. Liu, Y. Zhang, Z. Chen, X. Xu, L. Ye, Z. Wang, Y. Yang, D. Zhang and H. Zhu, *Sci. Adv.*, 2022, **8**, eabq4935.
28 C. M. Sullivan and L. Nienhaus, *Nanoscale*, 2023, **15**, 998–1013.
29 L. Nienhaus, J.-P. Correa-Baena, S. Wieghold, M. Einzinger, T.-A. Lin, K. E. Shulenberger, N. D. Klein, M. Wu, V. Bulović, T. Buonassisi, M. A. Baldo and M. G. Bawendi, *ACS Energy Lett.*, 2019, 888–895.
30 Z. A. VanOrman and L. Nienhaus, *ACS Energy Lett.*, 2021, **6**, 3686–3694.
31 Z. A. VanOrman, H. K. Drozdick, S. Wieghold and L. Nienhaus, *J. Mater. Chem. C*, 2021, **9**, 2685–2694.
32 A. Saha, K. V. Chellappan, K. S. Narayan, J. Ghatak, R. Datta and R. Viswanatha, *J. Phys. Chem. Lett.*, 2013, **4**, 3544–3549.
33 W. Wu, H. Guo, W. Wu, S. Ji and J. Zhao, *J. Org. Chem.*, 2011, **76**, 7056–7064.
34 Y. Y. Cheng, T. Khoury, R. G. C. R. Clady, M. J. Y. Tayebjee, N. J. Ekins-Daukes, M. J. Crossley and T. W. Schmidt, *Phys. Chem. Chem. Phys.*, 2010, **12**, 66–71.
35 Y. Y. Cheng, B. Fückel, T. Khoury, R. G. C. R. Clady, M. J. Y. Tayebjee, N. J. Ekins-Daukes, M. J. Crossley and T. W. Schmidt, *J. Phys. Chem. Lett.*, 2010, **1**, 1795–1799.
36 C. R. Brown, G. E. Eperon, V. R. Whiteside and I. R. Sellers, *ACS Appl. Energy Mater.*, 2019, **2**, 814–821.
37 F. Lang, N. H. Nickel, J. Bundesmann, S. Seidel, A. Denker, S. Albrecht, V. V. Brus, J. Rappich, B. Rech, G. Landi and H. C. Neitzert, *Adv. Mater.*, 2016, **28**, 8726–8731.
38 F. Lang, O. Shargaieva, V. V. Brus, H. C. Neitzert, J. Rappich and N. H. Nickel, *Adv. Mater.*, 2018, **30**, 1702905.
39 Y. Miyazawa, M. Ikegami, H.-W. Chen, T. Ohshima, M. Imaizumi, K. Hirose and T. Miyasaka, *iScience*, 2018, **2**, 148–155.
40 A. S. Bieber, C. M. Sullivan, K. E. Shulenberger, G. Moller, M. Mardani, S. Wieghold, T. Siegrist and L. Nienhaus, *J. Phys. Chem. C*, 2023, **127**, 4773–4783.

41 V. D'Innocenzo, G. Grancini, M. J. P. Alcocer, A. R. S. Kandada, S. D. Stranks, M. M. Lee, G. Lanzani, H. J. Snaith and A. Petrozza, *Nat. Commun.*, 2014, **5**, 3586.
42 M. I. Dar, G. Jacopin, S. Meloni, A. Mattoni, N. Arora, A. Boziki, S. M. Zakeeruddin, U. Rothlisberger and M. Grätzel, *Sci. Adv.*, 2016, **2**, e1601156.
43 A. Francisco-López, B. Charles, M. I. Alonso, M. Garriga, M. Campoy-Quiles, M. T. Weller and A. R. Goñi, *J. Phys. Chem. C*, 2020, **124**, 3448–3458.
44 K. Wu, A. Bera, C. Ma, Y. Du, Y. Yang, L. Li and T. Wu, *Phys. Chem. Chem. Phys.*, 2014, **16**, 22476–22481.
45 C. Greenland, A. Shnier, S. K. Rajendran, J. A. Smith, O. S. Game, D. Wamwangi, G. A. Turnbull, I. D. W. Samuel, D. G. Billing and D. G. Lidzey, *Adv. Energy Mater.*, 2020, **10**, 1901350.
46 C. Wehrenfennig, M. Liu, H. J. Snaith, M. B. Johnston and L. M. Herz, *APL Mater.*, 2014, **2**, 081513.
47 M. T. Weller, O. J. Weber, P. F. Henry, A. M. D. Pumpo and T. C. Hansen, *Chem. Commun.*, 2015, **51**, 4180–4183.
48 R. L. Milot, G. E. Eperon, H. J. Snaith, M. B. Johnston and L. M. Herz, *Adv. Funct. Mater.*, 2015, **25**, 6218–6227.
49 Y. Zhang, Y. Lei, Q. Zhang and Z. Xiong, *Org. Electron.*, 2014, **15**, 577–581.
50 I. Breen, R. Tempelaar, L. A. Bizimana, B. Kloss, D. R. Reichman and D. B. Turner, *J. Am. Chem. Soc.*, 2017, **139**, 11745–11751.
51 J. Li, Z. Chen, Q. Zhang, Z. Xiong and Y. Zhang, *Org. Electron.*, 2015, **26**, 213–217.
52 A. Ronchi and A. Monguzzi, *J. Appl. Phys.*, 2021, **129**, 050901.
53 S. Wieghold, A. S. Bieber, Z. A. VanOrman and L. Nienhaus, *J. Phys. Chem. Lett.*, 2019, 3806–3811.
54 R. A. Marcus, *Rev. Mod. Phys.*, 1993, **65**, 599–610.
55 A. Köhler and H. Bässler, *J. Mater. Chem.*, 2011, **21**, 4003–4011.
56 T. S. Lee, Y. L. Lin, H. Kim, B. P. Rand and G. D. Scholes, *Can. J. Chem.*, 2019, **97**, 465–473.
57 J. Chakkamalayath and P. V. Kamat, *J. Phys. Chem. C*, 2023, **127**, 16312–16318.
58 S. Wieghold, A. S. Bieber, Z. A. VanOrman, A. Rodriguez and L. Nienhaus, *J. Phys. Chem. C*, 2020, **124**, 18132–18140.
59 B. T. Diroll, *J. Phys. Chem. Lett.*, 2019, **10**, 5623–5628.
60 S. Tao, I. Schmidt, G. Brocks, J. Jiang, I. Tranca, K. Meerholz and S. Olthof, *Nat. Commun.*, 2019, **10**, 2560.
61 A. Monguzzi, J. Mezyk, F. Scotognella, R. Tubino and F. Meinardi, *Phys. Rev. B: Condens. Matter Mater. Phys.*, 2008, **78**, 195112.
62 C. R. Conti, A. S. Bieber, Z. A. VanOrman, G. Moller, S. Wieghold, R. D. Schaller, G. F. Strouse and L. Nienhaus, *ACS Energy Lett.*, 2022, 617–623.
63 D. G. Bossanyi, Y. Sasaki, S. Wang, D. Chekulaev, N. Kimizuka, N. Yanai and J. Clark, *JACS Au*, 2021, **1**, 2188–2201.
64 A. van der Lee, M. Polentarutti, G. H. Roche, O. J. Dautel, G. Wantz, F. Castet and L. Muccioli, *J. Phys. Chem. Lett.*, 2022, **13**, 406–411.
65 P. Coppens, O. Gerlits, I. I. Vorontsov, A. Yu. Kovalevsky, Y.-S. Chen, T. Graber, M. Gembicky and I. V. Novozhilova, *Chem. Commun.*, 2004, 2144–2145.
66 Y. Deng, L. Jiang, L. Huang and T. Zhu, *ACS Energy Lett.*, 2022, **7**, 847–861.
67 A. Haefele, J. Blumhoff, R. S. Khnayzer and F. N. Castellano, *J. Phys. Chem. Lett.*, 2012, **3**, 299–303.
68 G. Durocher and D. F. Williams, *J. Chem. Phys.*, 2003, **51**, 1675–1676.
69 J. Saltiel, G. R. March, W. K. Smothers, S. A. Stout and J. L. Charlton, *J. Am. Chem. Soc.*, 1981, **103**, 7159–7164.
70 S. Raišys, O. Adomėnienė, P. Adomėnas, A. Rudnick, A. Köhler and K. Kazlauskas, *J. Phys. Chem. C*, 2021, **125**, 3764–3775.
71 S. T. Hoffmann, J.-M. Koenen, U. Scherf, I. Bauer, P. Strohriegl, H. Bässler and A. Köhler, *J. Phys. Chem. B*, 2011, **115**, 8417–8423.
72 R. L. Milot, G. E. Eperon, H. J. Snaith, M. B. Johnston and L. M. Herz, *Adv. Funct. Mater.*, 2015, **25**, 6218–6227.
73 H. Sternlicht, G. C. Nieman and G. W. Robinson, *J. Chem. Phys.*, 1963, **38**, 1326–1335.